Isotopic ratio analysis of individual sub-micron particles via spICP-TOFMS

Sarah E. Szakas[1], Alexander Gundlach-Graham[1]

1. Department of Chemistry, Iowa State University, Ames, IA, USA
   Email: alexgg@iastate.edu

Abstract

We investigate the use of single particle inductively coupled plasma time-of-flight mass spectrometry (spICP-TOFMS) to measure isotopic ratios within individual sub-micron particles and explore the advantages and limitations of this method. Through the analysis of samarium (Sm) isotopes—^{147}Sm and ^{149}Sm—in individual monazite particles, and lead (Pb) isotopes – ^{206}Pb and ^{208}Pb – in individual galena particles, we demonstrate that isotope ratios recorded by spICP-TOFMS have precision controlled by Poisson statistics. This precision depends on the signal amount measured per isotope from an individual particle: as particle size increases, more counts of each isotope are detected, and the precision improves. In monazite particles with mass amounts of Sm from 40 ag to 4 fg, recorded isotope-ratio precision (relative standard deviation, RSD) ranged from 43% to 5%. However, the average isotope ratio from a particle population is still accurate; the molar ratio determined for ^{149}Sm/^{147}Sm was 0.912, which is within 1% of the expected ratio. Lead isotopic composition varies widely in nature because ^{206}Pb, ^{207}Pb, and ^{208}Pb are radiogenic isotopes that decay from thorium (Th) and uranium (U). In the analysis of lead isotopes from galena particles, we found that the RSD for ^{208}Pb/^{206}Pb ratio ranged from 32% to 2% for particles with 1.4 fg to 80 fg of Pb.

We further explore the use of spICP-TOFMS for radiometric dating of monazite particles. Monazite is used in geochronology for radiometric dating based on ^{208}Pb/^{232}Th and ^{206}Pb/^{238}U ratios. spICP-TOFMS analyses of individual monazite particles that contain only 0.02–80 fg of Th and 0.03 - 30 fg of U showed radiogenic Pb-isotope signatures and a median age of 550 Ma. We also show that the spread of ages from monazite particles is broader than explainable by Poisson statistics, revealing real variation in age or depletion/enrichment of Pb, Th, and/or U in the particles. Overall, we demonstrate that spICP-TOFMS can be used for accurate isotope-ratio analysis with precisions down to a few percent; however, understanding measurement noise is critical to define the significance of isotope ratios measured from individual particles.

Introduction

Isotope ratio measurements obtained by inductively coupled plasma mass spectrometry (ICP-MS) are utilized in many fields such as nuclear chemistry,[1,2] archeology and anthropology,[3,4] geochronology and geochemistry,[5,6] and environmental science.[7] ICP-MS offers high sensitivity, low detection limits (usually in the low parts per trillion level), large linear dynamic range, and straight-forward sample preparation. Compared to other mass spectral techniques, such as thermal ionization mass spectrometry (TIMS) and secondary ion mass spectrometry (SIMS), ICP-MS offers similar precision and accuracy while also providing higher throughput.[7,8] While precisions of ICP-MS with a quadrupole detector have been reported to have relative standard deviations (RSDs) of ≥0.1%, multi-collector (MC) ICP-MS can deliver isotope ratio RSDs down to 0.002% and lower,[9,10] and so these are the ICP-MS instruments of choice for precise and accurate isotope-ratio measurements. In conventional MC-ICP-MS isotope-ratio analyses, 'bulk' samples are homogenized and digested, and elements of interest may be isolated through chromatographic techniques before analysis by MC-ICP-MS. While this procedure results in stable isotopic signals and good precision, an obvious drawback is that only average isotopic composition of a sample is recorded; information on isotope variation within a sample is lost. In the context of geochronology, *in situ* analysis via laser-ablation (LA) MC-ICP-MS has increasingly become the standard method.[11,12] Many minerals important for radiometric dating (e.g. zircon, monazite) have pronounced zonation due to different growth stages, and thus can show variable ages across a single grain. The combination of mineral mapping with microscopy approaches or trace-element imaging by LA-ICP-MS, and single-spot analysis for isotope-ratio determination by LA-MC-ICP-MS allows for mineral- and zone-specific isotope-ratio dating.[6,13-15] More recently, whole mineral isotope imaging with LA-ICP-MS, has emerged as an approach to perform comprehensive *in-situ* dating of mineral samples.[16,17]

Multi-collector ICP-MS instruments provide substantially better isotope-ratio determination precision than quadrupole-based ICP-MS instruments because isotope signals are measured simultaneously at dedicated detectors and time-dependent correlated noise sources (e.g., plasma flicker, drift, etc.) can be eliminated through signal ratioing. However, the number of mass-to-charge ratios (*m/z*) detectable with a MC instrument is constrained by the physical number of detectors and the available relative *m/z*-range of ~15%.[18] State-of-the-art MC ICP-

MS instruments may be equipped with between 11-16 Faraday cup or electron multiplier detectors; the number and type of detectors used are determined based on analyte isotopes of interest and the sensitivity required to detect them.[19,20] On the other hand, to detect multiple isotopes across the whole elemental mass range quasi-simultaneously, a time-of-flight (TOF) mass analyzer can be used. In previous research, ICP-TOFMS has been characterized for isotope ratio analysis in terms of mass bias and isotope fractionation for light, mid-mass, and heavy isotopes: B, Sr, and Pb.[21] This study found that precision for $^{208}Pb/^{206}Pb$ was around 0.1% when a 1000 ng mL^{-1} solution of Pb was analyzed.[21] In other work, RSD values from 0.41 – 0.06% were obtained for analysis of $^{208}Pb/^{206}Pb$ ratios from Pb standards with concentrations from 1 to 100 ng mL^{-1}.[22] Both previously mentioned studies used 10 s acquisition times. With extended analysis times (up to 100 s), which produce more total ion counts, isotope ratio precisions for $^{107}Ag/^{109}Ag$ and for $^{151}Eu/^{153}Eu$ have been reported as low as 0.056 and 0.02%.[23,24] All mentioned studies on ICP-TOFMS isotopic analysis were carried out on dissolved samples.

In recent years, single-particle (sp) ICP-MS has emerged as powerful and high-throughput method to measure the particle number concentrations (PNCs), and element mass amounts in individual nanoparticles (<100 nm), sub-micron particles (<1000 nm), and microparticles.[25-27] In spICP-MS, a dilute suspension of particles is introduced into the ICP, where the particles are vaporized, atomized, and ionized. The resulting ion clouds are transmitted into the mass analyzer and *m/z*-specific particle-derived ion clouds are recorded as signal spikes by the MS detector. The particle-derived signal events are typically ~250-1000 µs in duration. With quadrupole-based mass analyzers, only one *m/z* can be quantitatively recorded per particle-derived signal.[28,29] However, with multi-channel mass analyzers, such as multi-collector sector-field or TOF mass analyzers, signals from multiple *m/z* can be recorded from an individual particle.[30-32] In particular, ICP-TOFMS instruments allow the collection of complete elemental mass spectra with sufficient time resolution to record single-particle events.[33] spICP-TOFMS has been used extensively to analyze mixtures of nano- and micro-particles from a wide range of environmental sample types. With spICP-TOFMS, many researchers aim to detect and classify natural and anthropogenic particles based on particle-type specific multi-element signatures.[34-38] Just as multi-element fingerprints allow for particle type classification, the analysis of isotope ratios of individual particles could be used to gain insights into particle origin.

To date, only a handful of researchers have reported the measurement of isotope ratios by spICP-MS. Yamashita et al. measured 30, 50, and 70 nm Pt NPs by single-particle MC-ICP-MS and demonstrated that RSD followed counting statistics and ranged from 40-10% for the smaller to larger Pt NPs. Similarly, Hendriks et al., reported $^{194}Pt/^{195}Pt$ ratios measured in 70 nm Pt NPs by spICP-TOFMS, though no isotope-ratio precision value was provided.[39] von der Au et al. and Aramendía et al. reported the use of isotope dilution combined with spICP-TOFMS to determine the sizes of Pt NPs and Ag NPs, respectively.[40,41] Montaño et al. reported Pb-isotope ratios determined by spICP-TOFMS from particles in boreal rivers in Canada.[42] Manard et al. and Tian et al. each investigated $^{107}Ag/^{109}Ag$ isotope ratio accuracy and precision measured via spICP-TOFMS and found that isotopic ratio precision is well described by Poisson counting statistics.[43,44] Finally, Bland et al. demonstrated that TiO_2 engineered nanoparticles enriched with ^{47}Ti could be used to track the fate and transport of anthropogenic TiO_2 particles against a natural particle background in soils through measurement of the $^{47}Ti/^{48}Ti$ ratio in individual particles by spICP-TOFMS.[45]

Here, we characterize the expected measurement variability in isotope-ratio measurements by spICP-TOFMS through the analysis of stable isotope ratios within two mineral samples: monazite ($REE(PO_4)$) and galena (PbS). We measure $^{149}Sm/^{147}Sm$ isotope ratios in monazite particles, $^{208}Pb/^{206}Pb$ ratios in galena particles, and explore the use of $^{208}Pb/^{206}Pb$ ratios to differentiate each mineral type. To further illustrate the capabilities of spICP-TOFMS for isotopic analysis, we measure $^{208}Pb/^{232}Th$ and $^{206}Pb/^{238}U$ ratios in the monazite particles to estimate their ages. We also developed Monte-Carlo Poisson confidence bands to account for the spread in spICP-TOFMS signal ratios due to Poisson noise. Based on these confidence bands, we can identify true isotope ratio outliers in our measured particle populations.

2. Methods and Materials:

2.1 Submicron Particle Suspensions Sample Preparation

Mineral samples used in this study include both monazite ($REE(PO_4)$) and galena (PbS).[46,47] The monazite sample arrived at our lab pre-ground. The original monazite sample was extracted from a rock sample containing a monazite crystal (acquired from Sieber and Sieber AG, Switzerland). Once extracted, the monazite was broken into smaller fragments, and those free of the original host rock were selected to be ball milled (4 min, Retsch Mixer Mill MM400).

About 10 mg of monazite powder was diluted into 50 mL ultrapure water (18.2 MΩ PURELAB flex, Elga LabWater, United Kingdom), vortexed for 60 seconds, and water bath sonicated for 10 minutes (VWR, PA, USA). An aliquot was then pipetted into a 2 mL Eppendorf tube (Eppendorf, Germany) and ultrasonicated with a program 10 s on, 5 s off for 60 s (100 W, VialTweeter, Hielscher UP200st, Germany). The suspension was allowed to settle for 10 minutes and aliquots were pipetted from the top for a subsequent ~4x dilution. This procedure was done so no large particles (i.e., particles with diameters > 3 μm that may not fully vaporize in the ICP) were sampled. The final particle number concentration (PNC) of the suspension used for analysis was ~4.3×10^5 particles mL^{-1}. While only one mineral stock suspension was prepared, two replicate spICP-TOFMS measurements (each with ~120 s data acquisition) were run.

A sample of galena was obtained via the Iowa State University Department of Geological and Atmospheric Sciences. The sample was ball milled (6 min, SPEX mixer/miller 8000M) and underwent the same sample preparation as the monazite suspension. The dilution of the particle suspension used for analysis had a spICP-TOFMS-determined PNC of ~9.29×10^4 particles mL^{-1}. Three replicate measurements (each with ~90 s of data acquisition) of the galena suspension were used for particle analysis.

All sample dilutions were prepared in ultrapure water spiked with Cs to a concentration of 5 ng mL^{-1}, as Cs is used in our analysis as an uptake standard to calculate transport efficiency with microdroplet calibration.

2.2 Analytical Instrumentation and Data Analysis

2.2.1 spICP-TOFMS

All data was acquired on an icpTOF-S2 instrument (TOFWERK AG, Thun, Switzerland). Suspended particles were transported to the instrument interface via a microFAST MC autosampler (Elemental Scientific, Omaha, NE, USA). In Table S1, we provide typical operating conditions of the ICP-TOFMS instrument.

Online microdroplet calibration was used to obtain matrix-matched calibration, to determine mass amounts of isotopes per particles, and to determine sample-specific PNCs.[48,49] Details of the online microdroplet calibration method have been reported previously.[48,50,51] Two calibration solutions were used for spICP-TOFMS analysis of the two mineral types. Both

solutions contain the same elements—Cs, Sm, Pb, Th, and U—but at different concentrations. Solutions were made gravimetrically from single-element standard solutions (High Purity Standards, Charleston, SC, USA) and prepared in 1% HNO_3 (w/v, in-house sub-boiled nitric acid, Savillex Corp, MN, USA). Importantly, the calibration solutions used in our experiments are element standards and not isotope standards, meaning they are unverified regarding isotopic abundances. The concentrations of isotopes within the microdroplet solution were calculated according to isotopic abundance values given by IUPAC.[52] Lack of use of isotopic standards may lead to systematic errors in the accuracy of determined isotope ratios and ages; however, use of element standards does not impact the discussion of precision of spICP-TOFMS measurements. In Table S2, we provide detailed parameters for the online microdroplet calibration measurements.

We analyzed spICP-TOFMS data with TOF-SPI (TOF Single-Particle Investigator),[53] an in-house batch analysis program created in LabVIEW (LabVIEW 2018, National Instruments, TX, USA). TOF-SPI calculates the critical value ($L_{C,sp,i}$) and the critical mass ($X^{mass}_{C,sp,i}$) of specified elements/isotopes (i). $L_{C,sp,i}$ is the count threshold criteria used to distinguish whether a signal is particle-derived or from the steady-state background. TOF-SPI background subtracts all particle data, corrects for split events, calculates absolute sensitivities, and determines PNCs and mass amounts of detected elements/isotopes within each particle. To ensure all spICP-TOFMS data are recorded within the linear working range of the ICP-TOFMS instrument, we remove all particle-derived signals with over 20,000 TofCts (summed counts from selected elements/isotopes used for analysis).[54] While monazite contains many rare earth elements (Ce, La, Nd, etc.), and all were detectable within the particles, we did not quantify these elements. Sulfur and phosphorous, which are major elements in galena and monazite, respectively, were not detectable at the single-particle level with our ICP-TOFMS tune settings, which were optimized for mid-to-high *m/z*.

2.2.3 Monte Carlo Simulations

Monte Carlo simulations of spICP-TOFMS signals were done with an in-house LabView Program to predict the signal structure of isotope ratios measured by spICP-TOFMS. In our simulation, a user inputs the number of particles, the median and standard deviation of the particle-size distribution, isotope mass fractions in the particles, sensitivities for each isotope (i),

and $L_{c,sp,i}$ values. The simulation then incorporates Poisson noise and outputs the expected particle-derived signals that would be measured in a spICP-TOFMS experiment. These Monte Carlo simulations represent the "best case," in which spICP-TOFMS signals are only limited by Poisson noise.

Monte Carlo Poisson confidence bands were also generated in LabVIEW. In this Monte Carlo approach, signals from two isotopes (A and B) with average rates (λ_A and λ_B), and a known signal ratio (λ_A/λ_B) are simulated. First, a series of average signal values (λ_A and λ_B) are created across a range of signal levels based on the known λ_A/λ_B ratio. Random draws ($N=10^5$) from Poisson distributions with means of λ_A and λ_B are then taken, and the ratios of these Poisson-sampled signals are obtained. For each λ_A and λ_B, the confidence intervals are established at the 2.5% and 97.5% percentiles of the Poisson-sampled signal ratios. Confidence bands at the 95% significance level are created by compiling the confidence intervals at all simulated λ_A and λ_B values. Confidence bands generated in the signal domain are converted to the amount (i.e., mass) domain using the absolute sensitivities for measured for isotopes A and B.

3. Results and Discussion

In this study, we aim to determine whether spICP-TOFMS is a viable technique to use for isotopic analysis, and to explore this method's advantages and limitations. In spICP-TOFMS analysis, the ability to accurately and precisely measure a given isotope's signal depends on its abundance within a particle, the critical mass required to detect the isotope (which depends on sensitivity and signal background levels), and detection noise. In the best-case scenario, particles will have a known size distribution, conserved isotope ratios, and Poisson noise will be the only uncorrelated noise source. In such a case, the measurement of ratios will be "Poisson-limited." However, even with these conditions, spICP-TOFMS measures a range of isotope ratios that vary as a function of particle size. To illustrate this, in Figure 1, we plot results from the Monte Carlo simulation of spICP-TOFMS signals from 100,000 particles with arbitrary isotopes, A and B. In our simulation, particles are modelled with a Log-Normal particle size distribution of 75*/1.5 nm,[55] a particle density of 5.15 g/mL, a conserved isotope ratio of 10/1 (A/B), absolute sensitivities of 1×10^{17} TofCts g^{-1} for both A and B, and equal critical values ($L_{c,sp}$ = 5 TofCts). The size and density parameters were selected to best replicate the real monazite mineral particles used in this study, and the other parameters were selected to simplify the explanation

and illustration of the data treatment for these simulated particles. Figure 1A is a graphical description of the Monte Carlo simulation for anticipated measured responses for isotopes A and B. As seen in Figure 1A, the whole mass distribution of the lower abundance isotope B is not measurable by spICP-TOFMS because many particles have mass amounts of B below the critical mass ($X^{mass}_{C,sp,B}$).

Throughout the manuscript, data will follow the format presented in Figure 1B and 1C. In Figure 1B, the simulated spICP-TOFMS signals of isotopes A and B are plotted to determine their correlation. Isotope signals are not measurable below their respective $L_{c,sp}$ values, and the relative uncertainty (i.e., the relative spread) of the measured signal ratio decreases as the intensity of the signals in the particles increase, i.e., as the sizes of the particles increase. Since Fig. 1B is on a log-log scale, only particle events with measurable amounts of both isotopes A and B are plotted. All spICP-TOFMS particle signal data is displayed in "TOF counts" (TofCts).[56] Data in the signal domain can be converted to mass, or molar, amounts using the determined isotope-specific sensitivities.

In Figure 1C, we provide a density scatter plot of the isotope signal ratios recorded from individual particles versus the signal of the major isotope. Understanding the shape and spread of data in this scatter plot is important for assessing spICP-TOFMS isotope-ratio performance. First, as seen in Figure 1C, no isotope ratio signals are measurable to the left of a defined boundary ($\mathrm{TofCts\ A}/L_{c,sp,B}$) because to the left of this line, signals of B have values below $L_{c,sp,B}$, and are therefore not detectable. This low-signal cutoff indicates that the measurable isotope ratio between A and B is particle-size (or isotope-abundance) dependent. Second, as the signals from particles increase (which corresponds to a larger diameter and more mass), the isotope signal ratios converge to the known ratio (here, 10/1 for A/B). The isotope-ratio is systematically biased in smaller particles; the contribution of the minor isotope is over-determined because at counts close $L_{C,sp}$, only signals from the upper tail of the signal distribution with added Poisson Noise are detectable. Finally, the confidence bands in Figure 1C show the majority of spread in the isotope-ratio data is explainable by Poisson-Normal statistics (black), but that Monte Carlo estimated Poisson confidence bands (green) provide an even better match with the spread of the isotope-ratio data. At low count rates ($\lambda < 5$), the Poisson-Normal approximation (in which confidence intervals are calculated with z-scores from Normal distribution with $\sigma = \lambda^{1/2}$) fails

because the distribution is highly skewed.[57-59] Monte Carlo Poisson confidence bands account for this skew and thus better match the spread of our spICP-TOFMS data. For particles with conserved isotope ratios, but variable sizes, our simulations show that few outliers are expected beyond the Monte Carlo Poisson confidence bands.

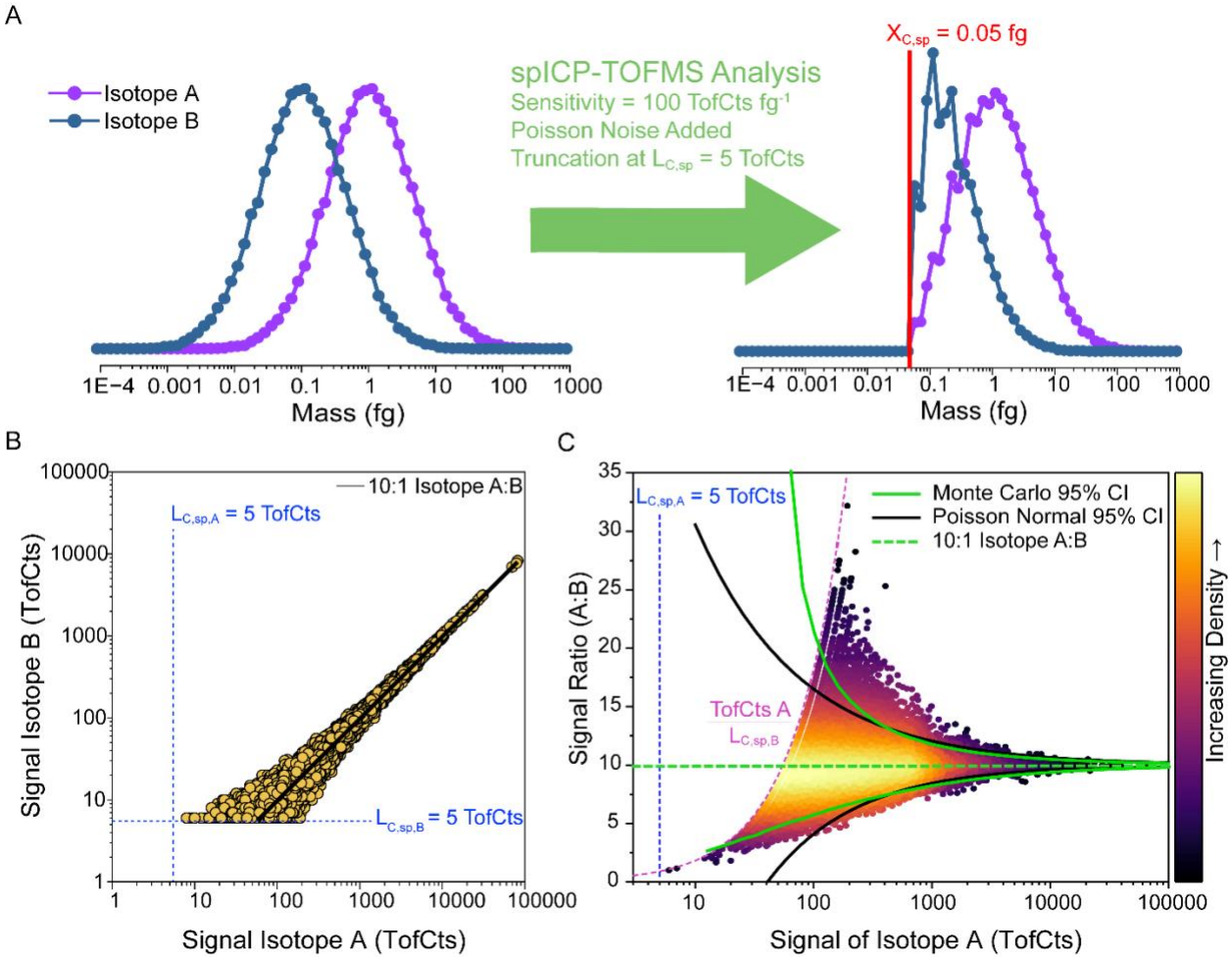

Figure 1. A) Schematic of the Monte Carlo simulation approach. The true mass distributions of two isotopes (A and B) are modelled and Poisson-distributed TOFMS signals are generated. Signals are truncated based on critical values ($L_{c,sp}$). **B)** Simulated spICP-TOFMS signals of isotope A versus isotope B from individual particles. The simulated particles show that isotope ratios converge to the specified, constant ratio of 10/1 (A/B). **C)** A density scatter plot of the signal ratio of isotopes A/B vs. signal of the major isotope A. While there is more spread in isotope ratios for particle events with low signal (i.e., from small particles), this spread is predictable and accounted for by Monte Carlo Poisson confidence bands. As particle mass increases, particles converge to the known isotope ratio.

3.1 Stable Isotope-Ratio Analysis by spICP-TOFMS

In experimental spICP-TOFMS data, just as with the simulated data, conserved isotope ratios in a population of particles are expected to converge to a single value and the spread of the ratios should be within the Monte Carlo Poisson confidence bands. To evaluate this hypothesis, spICP-TOFMS analyses of two isotope pairs from two unique mineral particle types were performed: $^{149}Sm/^{147}Sm$ in monazite and $^{208}Pb/^{206}Pb$ in galena.

Monazite is rich in many light rare earth elements, including Ce, La, Pr, Nd, and Sm, in addition to Th and U. For our analyses, we chose to quantify the isotope ratio of $^{149}Sm/^{147}Sm$ because these isotopes are moderately abundant in the particles and do not have any significant isobaric interferences. ^{149}Sm is a stable isotope with a molar abundance of 13.8%; ^{147}Sm is an extremely long-lived radio-isotope (half-life of 1.06×10^{11} years) with a natural molar abundance of 15.0%.[52] In Figure 2A, we plot the molar ratio of ^{149}Sm to ^{147}Sm recorded in the monazite particles. As seen, the measured molar ratio from the population of monazite particles is 0.91, which is within 1% of the expected natural $^{149}Sm/^{147}Sm$ ratio of 0.92. In Figure 2B, we plot the signal ratios of $^{149}Sm/^{147}Sm$ vs. the signal measured for ^{149}Sm. The $^{149}Sm/^{147}Sm$ TofCts ratio converges to 0.99, and the measured isotope-ratio population follows the same general shape as predicted by our Monte Carlo simulation (see Figure 1C). Likewise, the Monte Carlo Poisson confidence bands predict the spread of the isotope-ratio data.

In Figure 2C and 2D, we plot results from the analysis of Pb isotopes from individual galena particles. ^{206}Pb, ^{207}Pb and ^{208}Pb are radiogenic isotopes that are commonly used in fields such a geology, archeology, and aerosol science for applications such as radiometric dating and source apportionment.[60,61] Galena samples can have distinct Pb molar ratios of ^{208}Pb to ^{206}Pb based on their origin; however, the ratios of $^{208}Pb/^{206}Pb$ are expected to be close to ~2 and are typically consistent within a single sample. The galena sample we analyzed has a stable $^{208}Pb/^{206}Pb$ molar ratio of 1.86 (mass ratio of 1.88), as shown in Figure 2C. This molar ratio is consistent with others reported for galena.[62] The density scatter plot in Figure 2D differs slightly from the Sm isotope ratios shown in Figure 2B in that there are multiple spots with high density. These “hot spots” could indicate a multi-modal size distribution for the galena particles. While the size distribution of this particle population was not further confirmed with other techniques, these multiple areas of overlapping data points indicate the population detected is characterized

by multiple particle sizes. In our measurements, dissolved steady-state background measured in the galena samples prohibits the detection of small particles, which are expected to have higher PNCs in natural samples.[63] This limits the number and size of particles detected. It could be that a large population of small galena particles is undetected in our spICP-TOFMS analysis, which would, if detectable, show high density similar to the monazite particles in Figure 2B. Nonetheless, the spread in $^{208}Pb/^{206}Pb$ isotope-ratio data is effectively described by Monte Carlo Poisson confidence bands, which demonstrates that the isotope-ratio is constant in the galena particles.

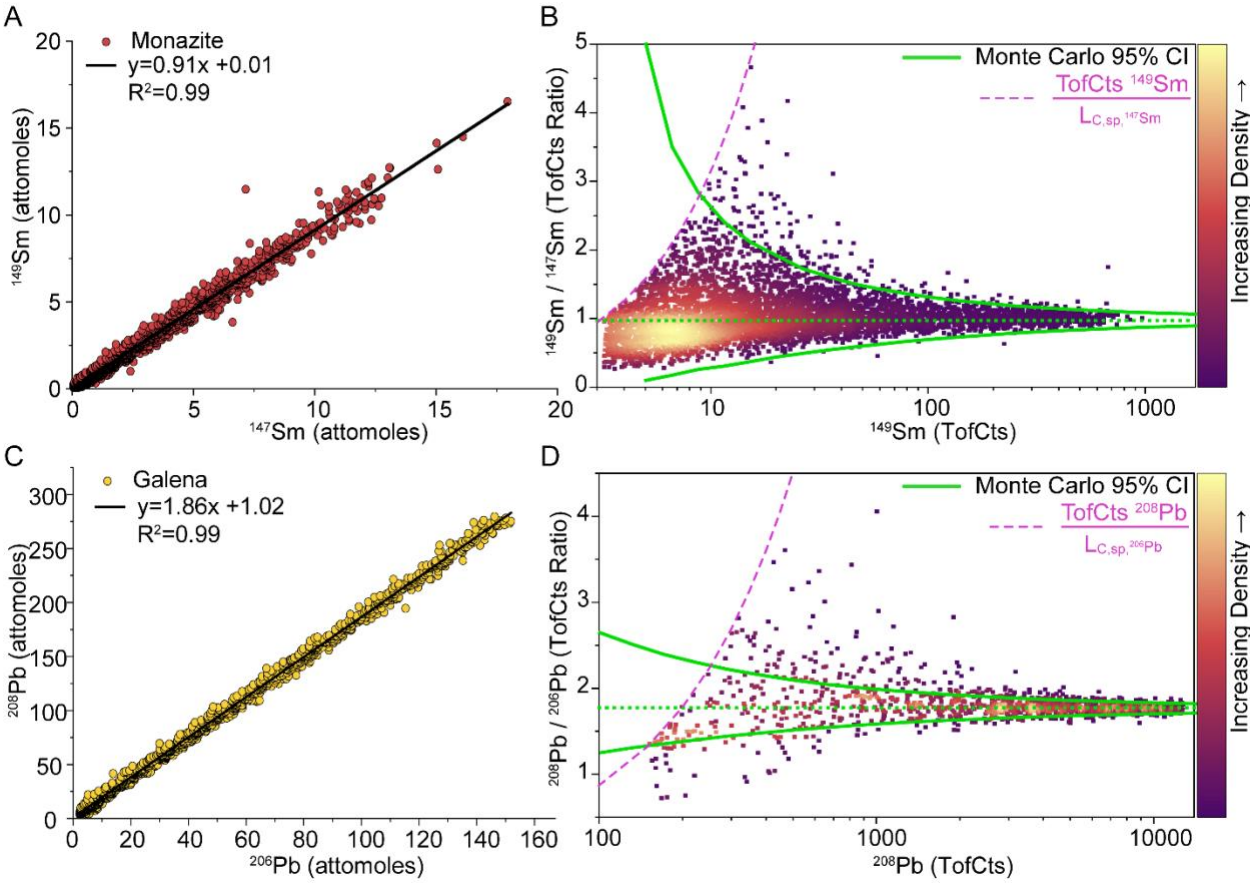

Figure 2. A) Sm isotopes are plotted against each other, and the slope of the linear fit represents the molar ratio detected within monazite particles. **B)** shows the count ratio of ^{149}Sm: ^{147}Sm with the Monte Carlo-Poisson CI and a density plot showing most of the particle ratios are detected within these bands. **C)** and **D)** display similar plots for the stable isotopes of ^{208}Pb to ^{206}Pb in galena mineral particles.

Precision in isotopic ratio analysis is usually reported as the RSD of the ratio over multiple sample measurements. In spICP-TOFMS, each measured particle is a sample, and the

RSD of the analysis depends on the particle size and isotope abundance. In Figure 3, we plot the RSD for $^{149}Sm/^{147}Sm$ and $^{208}Pb/^{206}Pb$ as a function of the determined mass of ^{149}Sm and ^{208}Pb, respectively. To obtain these plots, the logarithms (base 10) of particle-signal intensities of ^{149}Sm and ^{208}Pb were taken and binned at increments of 0.1. Isotope ratio precisions (i.e., RSDs) from data within the log-bins were then calculated. As seen in Figure 3a, the RSD of the $^{149}Sm/^{147}Sm$ ratio matches closely with that predicted by Poisson statistics. For the Sm isotopes, RSDs range from 43% to 5% for average TofCts from 10 to 800 for ^{149}Sm. The best precision we achieved was 5%; for an RSD of 2%, almost 5000 counts (i.e., 12 fg) of ^{149}Sm would be required. The initial increase in RSD for the $^{149}Sm/^{147}Sm$ ratio is an artifact in the data due to the low-signal cutoff for the ratio (i.e. $\mathrm{TofCts}\ {}^{149}\mathrm{Sm}/\mathrm{L}_{c,sp,{}^{147}\mathrm{Sm}}$) as seen in Figure 3A (pink dashed line). This cut-off restricts the range of isotope ratios able to be recorded and thus also restricts the range of deviations possible.

Unlike the Sm isotope-ratio precision, the RSD of $^{208}Pb/^{206}Pb$ from galena (see Figure 3B) deviates from the precision predicted by Poisson statistics, though the general trend of a lower RSD with larger particle size is followed. Deviation from the Poisson-predicted RSD could be partly caused by the low and inconsistent numbers of particles within each log-bin. The total PNC of the analyzed galena particles is ~5x less than that of the Sm-containing monazite particles. Additionally, the high background of ^{206}Pb and ^{208}Pb signals could introduce non-negligible noise that is propagated during background subtraction but are not accounted for in Poisson-predicted RSDs. This background noise causes the RSDs of the ratios to be elevated compared to the Poisson-predicted RSDs. Nonetheless, the measured precision for $^{208}Pb/^{206}Pb$ in these particles ranged from 32% to 2% for particles with 1.4 fg to 80 fg of Pb (which correspond to estimated particle diameters from 75 to 290 nm, assuming spherical shape and a density of 7.6 g mL^{-1}).[47] For spICP-TOFMS analysis, the maximum detectable cumulative isotopic signal in a single particle event is ~20,000 TofCts; above this signal level, the detector saturates, and the isotope-ratio is no longer quantitative. Thus, the lowest isotope-ratio precision at the single-particle level is ~1.4% (10k TofCts for each isotope). In our analysis of *in situ* $^{208}Pb/^{206}Pb$ ratios in galena particles, the 2% RSD achieved for the largest particles is near the performance limit of spICP-TOFMS.

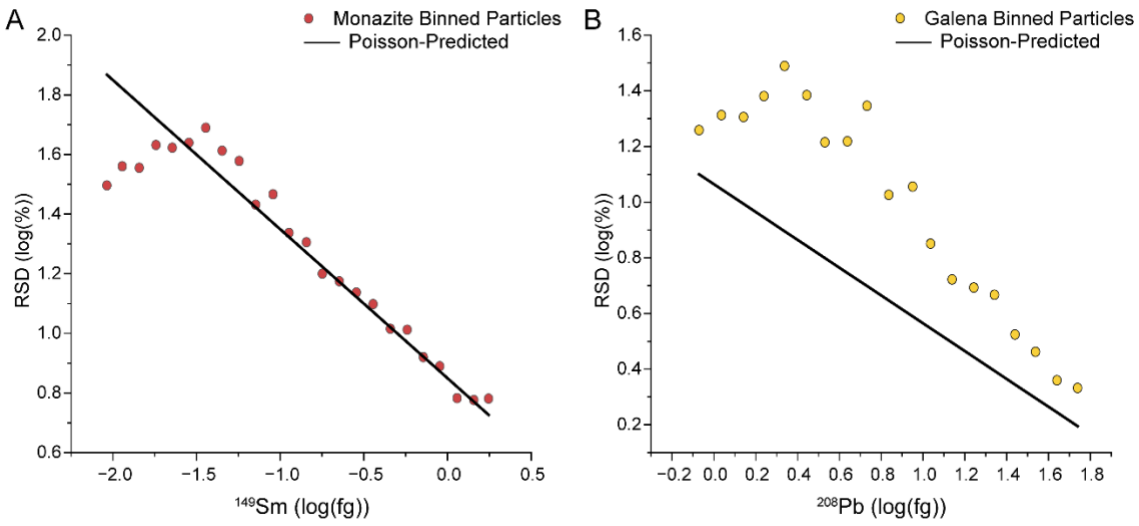

Figure 3. Log of RSDs obtained for spICP-TOFMS analysis of $^{149}Sm/^{147}Sm$ (A) and $^{208}Pb/^{206}Pb$ (B) from monazite and galena, respectively. RSDs are obtained for recorded isotope ratios of all particle data with masses of ^{149}Sm and ^{208}Pb binned logarithmically (base-10) at 0.1 increments. Poisson-predicted isotope ratio precisions are plotted as black lines.

3.2 Isotope-Ratio Fingerprinting by spICP-TOFMS

Single particle ICP-TOFMS enables the detection and quantification of multiple isotopes within individual particles and the rapid measurement of thousands of particles, making it a viable technique for isotope-fingerprinting of rare particle events. For example, this could be useful for source apportionment of aerosols,[64,65] or nuclear forensics.[66,67] In Figure 4, we present TOF mass spectra from the analysis of single particles of monazite and galena. As seen, the monazite particles have a radiogenic lead signature with a much higher relative abundance of ^{208}Pb compared to the 'natural' Pb isotope ratios recorded from galena particles and microdroplet standards. While the monazite particles contain detectable amounts of ^{206}Pb, ^{207}Pb, and ^{208}Pb, they lack sufficient amounts of non-radiogenic ^{204}Pb to be detected at the single-particle level. On the contrary, ^{204}Pb is detectable in ~68% of all galena multi-metal particles.

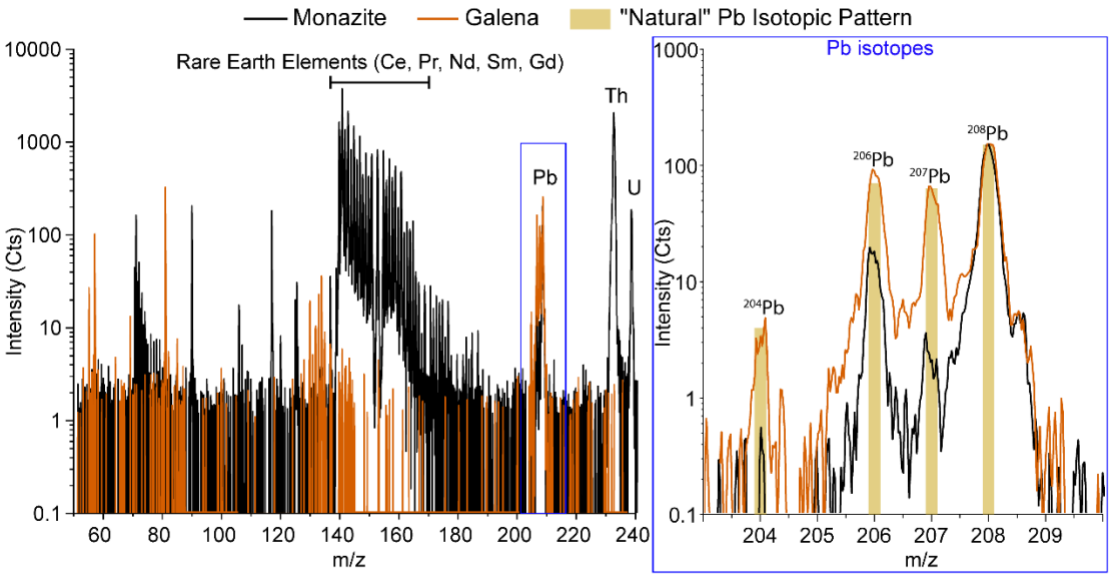

Figure 4. Full mass spectra (m/z 50-240) of individual particles of galena (orange) and monazite (black). The blue box zooms in on m/z 203-210 to show Pb isotopic signals. Yellow lines represent the relative abundances of each Pb isotope found within the microdroplets.

In Figure 5, we provide scatter plots of the mass ratios of $^{208}Pb/^{206}Pb$ recorded from monazite and galena particles. While the galena particles have a $^{208}Pb/^{206}Pb$ ratio that converges to ~2:1, the $^{208}Pb/^{206}Pb$ ratio in the monazite particles is much more scattered with a ratio that converges to ~10:1. While these two minerals can be identified based on other elements present in monazite (rare earth elements), this highlights the potential use of spICP-TOFMS to find isotopic enrichment within particles (for Pb and for other isotopes of interest) or for isotope fingerprinting applications. Single particle ICP-TOFMS requires low sample amounts, and particle-resolved isotope information provides more information than a bulk digest if mixtures of particle types are present.

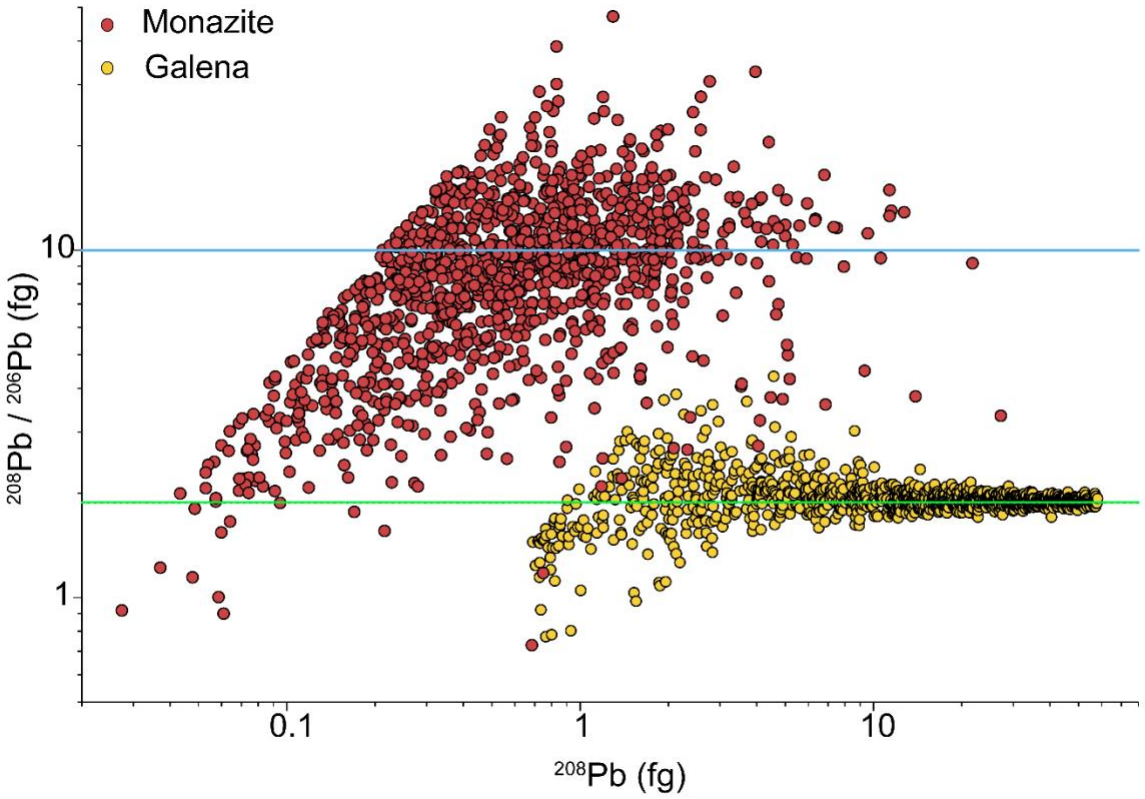

Figure 5. Mass ratios of ^{208}Pb/^{206}Pb measured within individual galena (yellow) and monazite (red) particles by spICP-TOFMS plotted versus the determined mass of ^{208}Pb in each particle. The monazite particles show more spread and converge to ratio of ~10:1 (blue line); the ^{208}Pb/^{206}Pb in the galena particles is more constrained and converges to ratio of ~2:1 (green line).

Monazite particles are rich in LREEs and Th, and can also contain significant amounts of U. The radiogenic Pb-isotope signatures detected in the monazite particles by spICP-TOFMS originate from the radioactive decay of ^{232}Th and ^{238}U to ^{208}Pb and ^{206}Pb, respectively. ^{208}Pb has a much higher abundance than ^{206}Pb because the monazite particles have ~20× more Th than U (see Figure S1). ^{207}Pb is also measured in the monazite particles and is the final decay product of ^{235}U; however, ^{235}U is not detectable in these particles, likely due to the low initial abundance of this isotope in the monazite and the shorter half-life of ^{235}U compared to ^{238}U. We further confirmed the presence of Pb, Th, and U in a limited number of monazite particles by SEM-EDS, which can be found in Figures S2-3. The clear radiogenic isotope signature of Pb in the monazite particles, along with the absence of non-radiogenic ^{204}Pb, indicates that these particles may be suitable for geochronological dating using the ^{232}Th-^{208}Pb and ^{238}U-^{206}Pb systems.

3.3 Application of sp-Isotopic Analysis to Geochronology

The decays of ^{232}Th to ^{208}Pb and ^{238}U to ^{206}Pb are commonly analyzed in monazite to determine the age of the minerals and better understand the conditions surrounding their formation.[68] Monazite incorporates significant amounts of Th and U during formation, but does not tend to incorporate Pb. Monazite grains have high thermal stability (closing temperature >800 °C) and are not very susceptible to radiation damage, which limits depletion of radiometric Pb.[69] The age of a monazite sample can be estimated from first-order decay of ^{232}Th and ^{238}U as shown in Equation 1,[70] where N is the number of atoms/moles of the parent isotope measured, N_0 is the number of atoms/moles originally present in the sample, λ is the rate constant, and t is time. In our spICP-TOFMS analysis of monazite particles, we did not detect ^{204}Pb even in particles with high mass amounts of other elements (indicating a large particle), thus we assume no "common" Pb was incorporated in the monazite grain at formation and that all ^{208}Pb is thorogenic and all ^{206}Pb is uranogenic. Assuming no initial amount of Pb, Equation 1 can be simplified as shown in Equation 2, using the ^{232}Th-^{208}Pb system as an example. The half-life ($t_{1/2}$) of ^{232}Th is around 14 billion years, whereas the half-life of ^{238}U is around 4.5 billion years.[71]

$$N = N_0 e^{-\lambda t} \text{ where } \lambda = \frac{\ln(2)}{t_{1/2}} \qquad \text{Equation 1}$$

$$\left(\frac{^{208}Pb}{^{232}Th}\right) = (e^{\lambda_{232} t} - 1) \qquad \text{Equation 2}$$

In our analyses, only spICP-TOFMS particle-derived signals with measurable amounts of ^{206}Pb and ^{238}U and/or ^{208}Pb and ^{232}Th were considered. Around 86% of multi-metal monazite particles contain measurable amounts of both ^{232}Th and ^{208}Pb; ~47% of these particles contain measurable amounts of ^{238}U and ^{206}Pb. In Figure 6, we provide density scatter plots of the Th-Pb and U-Pb ages determined for individual monazite particles with estimated diameters from 37 to 639 nm (assuming a density of 5.2 g cm^{-3} and an average monazite particle stoichiometry of $(Ce_{0.44}La_{0.14}Nd_{0.12}Pr_{0.08}Th_{0.23})PO_4$. In Figure S4, we provide a histogram comparing the recorded ages in the particles; Th-Pb and U-Pb systems both yield a median age of 550 Ma. As seen in Figure 6, while the determined single-particle Th-Pb and U-Pb ages converge to similar values, the spread of the determined ages is greater than predicted by Poisson statistics and does not match the shape expected for homogenous isotope ratios (see Figure 1). Particles with measured

isotope ratios that fall outside the Monte Carlo Poisson confidence bands likely do not belong to the same particle population with an age that converges to ~550 Ma. These outlier monazite particles could be the result of true age differences via zonation of monazite grains,[68] or could be due to the depletion or enrichment of Pb, Th, or U from processes such as chemical weathering. For example, monazite particles with depleted Pb would appear younger, whereas particles enriched in Pb would appear older. Particles could also have "common lead" that the radiogenic Pb signal was not normalized against, as ^{204}Pb was not detectable, which would alter the ages measured. Regardless of the physical cause of outlier ages, our spICP-TOFMS analysis demonstrates that these outliers are not analytical artifacts and that the precision achievable for dating sub-micron particles by spICP-TOFMS is not solely limited by Poisson statistics of spICP-TOFMS measurements, but also by true heterogeneity of the particles analyzed.

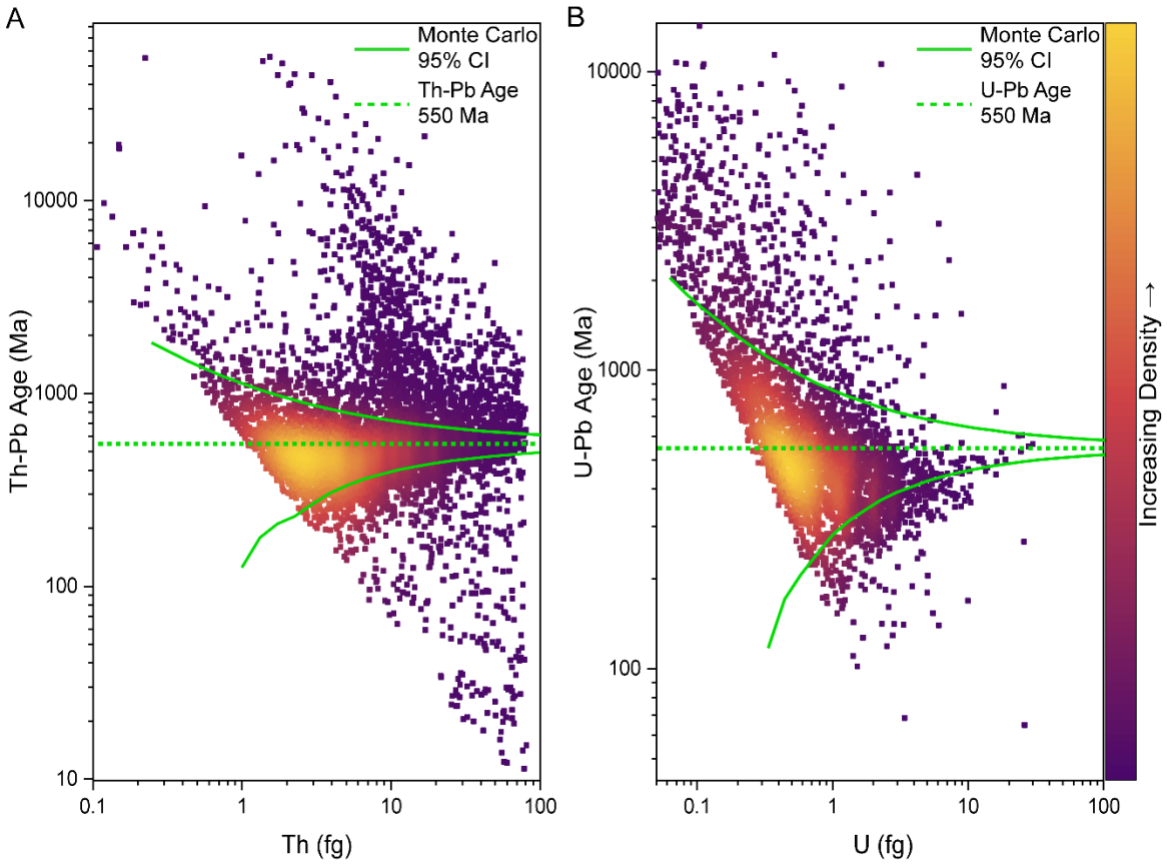

Figure 6. Determined ages of individual monazite particles from the Th-Pb system (A) and U-Pb system (B) plotted against the mass of either Th or U, respectively. As particle mass increases, isotope ratios of ^{208}Pb/^{232}Th and ^{206}Pb/^{238}U converge to a single value, and this corresponds to a single determined age. The median age for both systems is determined to be 550 Ma (green dotted line). While most determined ages fall within the Monte-Carlo Poisson confidence bands

(green lines), the determined ages have spread larger than that explainable by analytical uncertainty of the measurement.

Conclusions

We demonstrated that spICP-TOFMS can perform isotope-ratio analysis of individual sub-micron particles; however, the relatively low signals measurable from single particles caps the Poisson-limited isotope-ratio precision at ~1.4%. For small particles with low counts of analyte isotopes, isotope-ratio precisions greater than 10% are common. With Monte Carlo simulations and the analysis of stable Sm and Pb isotopes, we demonstrate that the spread in spICP-TOFMS-determined isotope-ratios is predictable and dominated by Poisson error. For monazite particles, $^{149}Sm/^{147}Sm$ RSD ranged from 43% to 5%. Similarly, for galena particles, $^{208}Pb/^{206}Pb$ RSD ranged from 32% to 2%. The large spread in RSD highlights that isotope-ratio analyses of individual particles by spICP-TOFMS should always consider the mass amounts of the isotopes measured. When the mass amounts of isotopes of interest are low within particles, the precision of the analysis may limit the ability to determine accurate ratios and identify particles with anomalous ratios.

We also demonstrate, for the first time, the radioisotope dating of individual monazite particles by spICP-TOFMS through the analysis of $^{208}Pb/^{232}Th$ and $^{206}Pb/^{238}U$ isotope ratios. We determined that the age of our sample is approximately 550 Ma. The determined age is most likely inaccurate, as we did not confirm the age through other techniques or use isotopic standards for the analysis. Nonetheless, our results show that spICP-TOFMS provides sufficient sensitivity to determine reasonable ages at the single-particle level. Since dating of individual particles requires the use of isotopic ratios, accurate spICP-TOFMS dating requires the analysis of large particles. For example, to obtain less than a 5% RSD on the predicted age of monazite particles, we would need to measure particles with at least ~60 fg of Th. The upper limit on the precision available for spICP-TOFMS is defined by TOFMS detector saturation, and so extension of the linear dynamic range to measure more signal per isotope per particle would improve RSDs achievable.

While RSDs achievable by spICP-TOFMS are significantly higher than those reported with MC-ICPMS, the spread around the spICP-TOFMS-determined ratios is predictable and

explainable via Poisson statistics. For the analysis of monazite particles, we demonstrate that many of the determined $^{208}Pb/^{232}Th$ and $^{206}Pb/^{238}U$ ratios have variability greater than analytical uncertainty, and thus the precision of the overall analysis is dictated by particle heterogeneity. Isotope-ratio analysis by spICP-TOFMS is a simple and rapid means of analyzing multiple isotope ratios for large populations of particles. Altogether, this could make spICP-TOFMS well suited for application in fields in which isotope ratios have large variability, such as in the source apportionment of aerosols or in nuclear forensics.

Conflicts of interest

The authors do not have any conflicts of interest to declare.

Acknowledgements

The authors would like to acknowledge Iowa State University for funding through a faculty start-up grant, and funding though NSF CAREER grant CHE-2237291. We would also like to thank Dr. Ralf Kaegi at EAWAG for the monazite sample, as well as the Iowa State University Department of Geological and Atmospheric Sciences for the galena mineral sample. We would like to thank Hark Karkee, Aishwarya Mantravadi, and Dr. Yulia Zaikina from the Department of Chemistry at Iowa State University for ball-milling of the galena mineral. We also want to acknowledge the Iowa State University Glass Shop and Chemistry Machine Shop for fabrication of our microdroplet introduction system.

References

1. S. Boulyga, S. Konegger-Kappel, S. Richter and L. Sangély, *J. Anal. At. Spectrom.*, 2015, **30**, 1469-1489.
2. V. C. Bradley, T. L. Spano, S. C. Metzger, B. W. Ticknor, D. R. Dunlap, N. A. Zirakparvar, B. D. Roach, C. R. Hexel and B. T. Manard, *Anal Chim Acta*, 2022, **1209**, 339836.
3. E. J. Bartelink and L. A. Chesson, *Forensic Sci Res*, 2019, **4**, 29-44.
4. A. M. Ghazi, *Appl. Geochem.*, 1994, **9**, 627-636.
5. B. Eglington, M. Fayek and T. K. Kyser, *Applied Isotope Geochemistry*, Mineralogical Association of Canada, 2019.
6. A. M. Cruz-Uribe, G. Craig, J. M. Garber, B. Paul, C. Arkula and C. Bouman, *Geostand Geoanal Res.*, 2023, **47**, 795-809.
7. V. Balaram, W. Rahaman and P. Roy, *GeoGeo*, 2022, **1**, 100019.
8. J. S. Becker and H.-J. Dietze, *Fresenius J. Anal. Chem.*, 2000, **368**, 23-30.
9. F. Vanhaecke, L. Balcaen and D. Malinovsky, *J. Anal. At. Spectrom.*, 2009, **24**, 863-886.
10. K. G. Heumann, S. M. Gallus, G. Radlinger and J. Vogl, *J. Anal. At. Spectrom.*, 1998, **13**, 1001-1008.
11. T. Hirata and T. Ohno, *J. Anal. At. Spectrom.*, 2001, **16**, 487-491.

12. P. J. Sylvester, *Geostandards and Geoanalytical Research*, 2008, **32**, 469-488.
13. D. J. Goudie, C. M. Fisher, J. M. Hanchar, J. L. Crowley and J. C. Ayers, *Geochem., Geophys., Geosyst.*, 2014, **15**, 2575-2600.
14. T. Iizuka, S. M. Eggins, M. T. McCulloch, L. P. J. Kinsley and G. E. Mortimer, *Chem. Geol.*, 2011, **282**, 45-57.
15. Y. Jiang, S. V. Hohl, X. Huang and S. Yang, *Geoscience Frontiers*, 2024, **15**, 101736.
16. D. M. Chew, J. A. Petrus, G. G. Kenny and N. McEvoy, *J. Anal. At. Spectrom.*, 2017, **32**, 262-276.
17. D. Chew, K. Drost, J. H. Marsh and J. A. Petrus, *Chemical Geology*, 2021, **559**, 119917.
18. N. Jakubowski, T. Prohaska, L. Rottmann and F. Vanhaecke, *J. Anal. At. Spectrom.*, 2011, **26**, 693-726.
19. Thermo Fisher Scientific Inc., *Neoma Multicollector ICP-MS - Illuminating the edge of discovery*, 2020.
20. Nu Instruments Limited, *Plasma 3 Multi-Collector ICP-MS*, 2022.
21. A. Retzmann, S. Faßbender, M. Rosner, M. von der Au and J. Vogl, *J. Anal. At. Spectrom.*, 2023, **38**, 2144-2158.
22. M. Ohata and H. Hagino, *Int. J. Mass Spectrom.*, 2018, **430**, 31-36.
23. P. P. Mahoney, S. J. Ray and G. M. Hieftje, *Appl. Spectrosc.*, 1997, **51**, 16A-28A.
24. L. Hendriks, A. Gundlach-Graham, B. Hattendorf and D. Günther, *J. Anal. At. Spectrom.*, 2017, **32**, 548-561.
25. M. D. Montaño, J. W. Olesik, A. G. Barber, K. Challis and J. F. Ranville, *Anal. Bioanal. Chem.*, 2016, **408**, 5053-5074.
26. D. Mozhayeva and C. Engelhard, *J. Anal. At. Spectrom.*, 2020, **35**, 1740-1783.
27. Z. Meng, L. Zheng, H. Fang, P. Yang, B. Wang, L. Li, M. Wang and W. Feng, *Processes*, 2023, **11**.
28. M. D. Montaño, H. R. Badiei, S. Bazargan and J. F. Ranville, *Environ. Sci.: Nano*, 2014, **1**, 338-346.
29. S. Naasz, S. Weigel, O. Borovinskaya, A. Serva, C. Cascio, A. K. Undas, F. C. Simeone, H. J. P. Marvin and R. J. B. Peters, *J. Anal. At. Spectrom.*, 2018, **33**, 835-845.
30. T. Hirata, S. Yamashita, M. Ishida and T. Suzuki, *Mass Spectrom (Tokyo)*, 2020, **9**, A0085.
31. S. Yamashita, M. Ishida, T. Suzuki, M. Nakazato and T. Hirata, *Spectrochim. Acta, Part B*, 2020, **169**, 105881.
32. S. Yongyang, W. Wei, L. Zhiming, D. Hu, Z. Guoqing, X. Jiang and R. Xiangjun, *J. Anal. At. Spectrom.*, 2015, **30**, 1184-1190.
33. A. Gundlach-Graham, in *Analysis and Characterisation of Metal-Based Nanomaterials*, Elsevier, 2021, DOI: 10.1016/bs.coac.2021.01.008, pp. 69-101.
34. A. Praetorius, A. Gundlach-Graham, E. Goldberg, W. Fabienke, J. Navratilova, A. Gondikas, R. Kaegi, D. Günther, T. Hofmann and F. von der Kammer, *Environ. Sci.: Nano*, 2017, **4**, 307-314.
35. F. Loosli, J. Wang, S. Rothenberg, M. Bizimis, C. Winkler, O. Borovinskaya, L. Flamigni and M. Baalousha, *Environ. Sci.: Nano*, 2019, **6**, 763-777.
36. K. Mehrabi, R. Kaegi, D. Günther and A. Gundlach-Graham, *Environ. Sci.: Nano*, 2021, **8**, 1211-1225.
37. T. R. Holbrook, D. Gallot-Duval, T. Reemtsma and S. Wagner, *J. Anal. At. Spectrom.*, 2021, **36**, 2684-2694.

38. G. D. Bland, M. Battifarano, Q. Liu, X. Yang, D. Lu, G. Jiang and G. V. Lowry, *Environ. Sci. Technol.*, 2022, **10**, 1023-1029.
39. L. Hendriks, R. Bruenjes, S. Taskula, J. Kocic, B. Hattendorf, G. Bland, G. Lowry, E. Bolea-Fernandez, F. Vanhaecke, J. Wang, M. Baalousha, M. von der Au, B. Meermann, T. R. Holbrook, S. Wagner, S. Harycki, A. Gundlach-Graham and F. von der Kammer, *Nanoscale*, 2023, **15**, 11268-11279.
40. M. von der Au, S. Faßbender, M.-I. Chronakis, J. Vogl and B. Meermann, *J. Anal. At. Spectrom.*, 2022, DOI: 10.1039/D2JA00072E.
41. M. Aramendía, D. Leite, J. Resano, M. Resano, K. Billimoria and H. Goenaga-Infante, *Nanomaterials (Basel)*, 2023, **13**.
42. M. D. Montaño, C. W. Cuss, H. M. Holliday, M. B. Javed, W. Shotyk, K. L. Sobocinski, T. Hofmann, F. v. d. Kammer and J. F. Ranville, *ACS Earth and Space Chemistry*, 2022, **6**, 943-952.
43. B. T. Manard, V. C. Bradley, C. D. Quarles, L. Hendriks, D. R. Dunlap, C. R. Hexel, P. Sullivan and H. B. Andrews, *Nanomaterials*, 2023, **13**, 1322.
44. X. Tian, H. Jiang, M. Wang, W. Cui, Y. Guo, L. Zheng, L. Hu, G. Qu, Y. Yin, Y. Cai and G. Jiang, *Anal. Chim. Acta*, 2023, **1240**, 340756.
45. G. D. Bland, P. Zhang, E. Valsami-Jones and G. V. Lowry, *ACS ES&T*, 2022, **56**, 15584-15593.
46. K. J. Murata, H. J. Rose and M. K. Carron, *Geochim. Cosmochim. Acta*, 1953, **4**, 292-300.
47. Galena, https://www.mindat.org/min-563.html, (accessed July, 2024).
48. K. Mehrabi, D. Günther and A. Gundlach-Graham, *Environ. Sci.: Nano*, 2019, **6**, 3349-3358.
49. A. Gundlach-Graham and K. Mehrabi, *J. Anal. At. Spectrom.*, 2020, **35**, 1727-1739.
50. S. Harycki and A. Gundlach-Graham, *Anal Bioanal Chem*, 2022, **414**, 7543-7551.
51. L. Hendriks, B. Ramkorun-Schmidt, A. Gundlach-Graham, J. Koch, R. N. Grass, N. Jakubowski and D. Günther, *J. Anal. At. Spectrom.*, 2019, **34**, 716-728.
52. J. R. d. Laeter, J. K. Böhlke, P. D. Bièvre, H. Hidaka, H. S. Peiser, K. J. R. Rosman and P. D. P. Taylor, *Pure Appl. Chem.*, 2003, **75**, 683-800.
53. A. Gundlach-Graham, S. Harycki, S. E. Szakas, T. L. Taylor, H. Karkee, R. L. Buckman, S. Mukta, R. Hu and W. Lee, *J. Anal. At. Spectrom.*, 2024, DOI: 10.1039/D3JA00421J.
54. H. Karkee and A. Gundlach-Graham, *Environ Sci Technol*, 2023, **57**, 14058-14070.
55. E. Limpert, W. A. Stahel and M. Abbt, *BioScience*, 2001, **51**, 341-352.
56. A. Gundlach-Graham and R. Lancaster, *Anal. Chem.*, 2023, **95**, 5618-5626.
57. E. L. Crow and R. S. Gardner, *Biometrika*, 1959, **46**, 441-453.
58. L. Barker, *The American Statistician*, 2002, **56**, 85-89.
59. M. B. Swift, *Communications in Statistics - Theory and Methods*, 2009, **38**, 748-759.
60. J. Milot, J. Blichert-Toft, M. A. Sanz, N. Fetter, P. Télouk and F. Albarède, *Chem. Geol.*, 2021, **583**, 120444.
61. J. Longman, D. Veres, V. Ersek, D. L. Phillips, C. Chauvel and C. G. Tamas, *Sci. Rep.*, 2018, **8**, 6154.
62. X.-K. Zhu, J. Benefield, T. B. Coplen, Z. Gao and N. E. Holden, *Pure and Applied Chemistry*, 2021, **93**, 155-166.
63. A. J. Goodman, A. Gundlach-Graham, S. G. Bevers and J. F. Ranville, *Environ. Sci.: Nano*, 2022, **9**, 2638-2652.

64. J. R. Graney, E. S. Edgerton and M. S. Landis, *Science of The Total Environment*, 2019, **654**, 1293-1304.
65. S. S. Kienast, G. Winckler, J. Lippold, S. Albani and N. M. Mahowald, *Global Biogeochemical Cycles*, 2016, **30**, 1526-1541.
66. X. Z. Zhang, F. Esaka, K. T. Esaka, M. Magara, S. Sakurai, S. Usuda and K. Watanabe, *Spectrochim. Acta, Part B*, 2007, **62**, 1130-1134.
67. F. Esaka, D. Suzuki and M. Magara, *Anal. Chem.*, 2015, **87**, 3107-3113.
68. M. J. Kohn and J. D. Vervoort, *Geochemistry, Geophysics, Geosystems*, 2008, **9**.
69. T. Yan, D. Liu, C. Si and Y. Qiao, *Minerals*, 2020, **10**, 239.
70. B. Schoene, in *Treatise on Geochemistry (Second Edition)*, eds. H. D. Holland and K. K. Turekian, Elsevier, Oxford, 2014, DOI: 10.1016/B978-0-08-095975-7.00310-7, pp. 341-378.
71. W. L. Newman, *Geologic time*, 1997.